

The Correlation of Electrical Properties of Prestressed Unimorphs as a Function of Mechanical Strain and Displacement

R. G. Bryant,¹ K. M. Mossi,² J. A. Robbins,² and B. F. Bathel³

¹NASA Langley Research Center, MS 226, Hampton, VA 23681, USA

²Virginia Commonwealth University, Department of Engineering, Richmond, VA 23294, USA ³NASA LaRC USRP, University of Iowa, Department of Mechanical Engineering, Iowa City, IA 52242, USA

ABSTRACT

Prestressed Unimorph-type actuators are being adapted for industrial applications previously not envisioned for piezoelectric based technology. These include electronically controlled diesel valve injectors, non-resonance fluidic pumps and low-stroke linear motors. To expand the range of applications and refine the design of these actuators for additional technologies, the effects of load placement, force distribution and mounting must be investigated in order to retrofit existing devices and systems. This research uses several sets of multi-strain gauged THUNDER actuators mounted in a fully compliant test fixture equipped with an LVDT and weight system and to characterize the room temperature strain and displacement as a function of mechanical loading. The results will be used to refine computational models that aid in the design of these actuators for future applications.

Keywords: Piezoelectric actuators; PZT strain; THUNDER; NASA actuators

INTRODUCTION

The THUNDER actuator, developed by researchers at NASA Langley, is a mechanically prestressed piezoelectric ceramic package [1, 2]. The mechanical prestress generated by a thermal mismatch (Coefficient of Thermal Expansion [CTE]) of the different materials used to create the laminated structure. Compared to flat plate electroactive ceramics, these prestressed actuators have several parameters that experience a greater degree and rate of change as a function

Received December 21, 2004; In final form February 3, 2005.

*Corresponding author. E-mail: robert.g.bryant@nasa.gov

of either loading as a spring, or during actuation as a fulcrum-lever. For instance, the piezoelectric “d” values change nonlinearly with increasing electric field, and are not relevant in describing these electro-mechanical benders. Spring constants and displacement, rather than modulus and strain, are better descriptors for THUNDER. Additionally, actuator topography, boundary conditions and the effects of stress-induced domain switching warrant consideration.

There are several papers that have discussed the mathematical modeling of this actuator [3–11]. Although these articles approximate the experimental results on a limited scale, they demonstrate the need for additional experimental work to refine the THUNDER computational model. An accurate generalized predictive model does not exist for THUNDER for several reasons; much of the experimental baseline data has been taken with arbitrary experimental boundary conditions, a rigorous comparison of areal strain and displacement has not been done, and some assumptions used to model the behavior of this device (Hooke’s Law, “d” constants and open/closed circuit elastic values) are less relevant than previously thought. Hence, no baseline archetype exists that can be tailored to address specific engineering problems. This is the first in a series of papers that present some of the initial experimental data needed to refine the computational models that describe the behavior of the THUNDER actuator. This initial work presents the isostatic (time independent) behavior of a series of commercially available THUNDER wafers and compares their areal XY strains and displacements as a function of open and short circuit conditions versus applied loads and DC electric fields [12]. These loads and electric fields range from 0 to tens of Newtons and 0 to several kV/mm respectively at room temperature. The electric field and strain results are compared to those for a flat PZT plate taken under the same experimental conditions.

EXPERIMENTAL

Equipment

The THUNDER X-R series wafers were obtained from FACE International Corp. (Norfolk, VA), and the XY-strain gauges, CEA-13-032WT-120, and related supplies were purchased from Vishay Micro-Measurements Group (Raleigh, NC). All computerized data acquisition (DAQ) hardware was acquired from National Instruments “NI” (Austin TX) and run under LabView 7.1 software.

Procedure

The surface topology of each type of Series-R THUNDER wafer was measured using a Fanamation 606040 coordinate axis machine to 8.1 μm accuracy. The surfaces of THUNDER wafers were lightly sanded with 400 grit emery paper and cleaned with isopropanol. The strain gauges were arranged in a

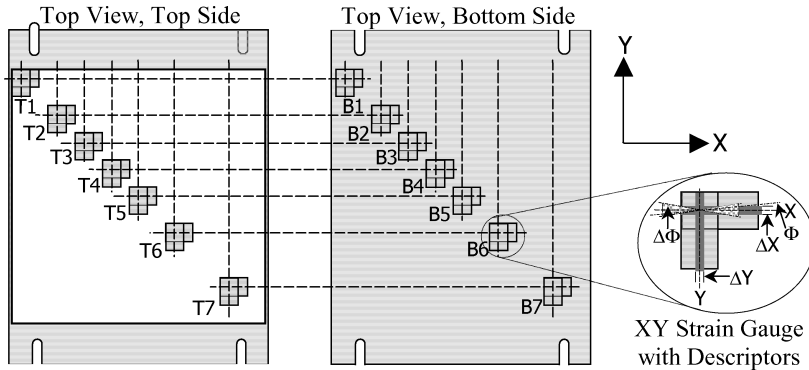


Figure 1. Top-down view of THUNDER 6-R with gauge work.

predetermined pattern, held in place with cellophane tape, and the backsides were treated with M-Bond Catalyst C. The gauges were then transferred to the top and bottom surfaces of the THUNDER wafers and bonded in place with Vishay M-Bond 200 acrylic adhesive, according to the supplier's instructions. The cellophane tape was removed and the actual location and off-axis rotation of each bonded gauge were measured (Fig. 1). Wires were soldered to the gauge pads and the resistance was measured to confirm operational performance.

The wafers were then mounted in a freely rolling single cantilever slide fixture and the gauges were wired into NI SCXI-1394 terminal blocks, (quarter bridge configuration) connected to NI SCXI 1520 8-channel Universal Strain Modules housed in a NI SCXI-1000 4 slot chassis, providing 32 total channels. The system was run using NI LabView 7.1 software interfaced through a NI 6036E PCMCIA DAQ card. Voltage was supplied to the wafers using a TREK 609E-6 Amp driven by an Agilent 33120A function generator operating in DC mode. The current and voltage outputs were confirmed using a Tektronics 1002 O-Scope connected to the TREK amplifier output monitors. Uniform loads were applied to the free end of the test frame by hanging weights from the rolling supported mount of the fixture. The wafer's center displacement was determined from a Trans-Tek LVDT model 0237-0000 by reading the LVDT voltage and calculating the relative displacement (0 V being the wafer at rest) from a calibration curve.

RESULTS AND DISCUSSION

THUNDER Device

The commercial THUNDER wafer is a mechanically prestressed laminate structure. As shown in Figs. 2a–b and 3, the device consists of 5 layers, the bottom

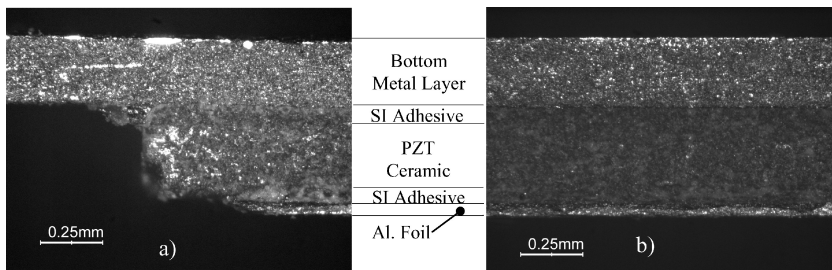


Figure 2. Diced cross sections of THUNDER wafer, (a) End view and (b) Midsection.

metallic prestress layer, a layer of LaRC-SI polyimide adhesive, the electroded and poled PZT ceramic, another layer of LaRC-SI adhesive and a top layer of knurled aluminum foil. A commercial THUNDER 7-Rx wafer is shown in Figure 4.

Figures 2a and 3 show the edge profiles of the resulting laminate. The decrease in area of successive layers helps mitigate electrical shorting during actuation. The bottom layer affords a platform to attach mounting fixtures. After the wafers are laminated and inspected, wires are attached (silver epoxy or solder) to each metal surface and they are poled (positive topside) in a dielectric fluid at approximately 3.5 kV/mm at ambient temperature for 1 minute, prior to delivery.

Since wafers are poled in the “3” or “Z” direction, the wafer expands and contracts about this axis when voltage is applied along or against the poled direction, respectively. This expansion or contraction, along the “3” direction, results in the opposite contraction or expansion along the orthogonal “1” and “2” axes or XY-plane. This secondary effect causes the wafer to displace in the negative Z-direction, from rest, as a positive voltage is applied.

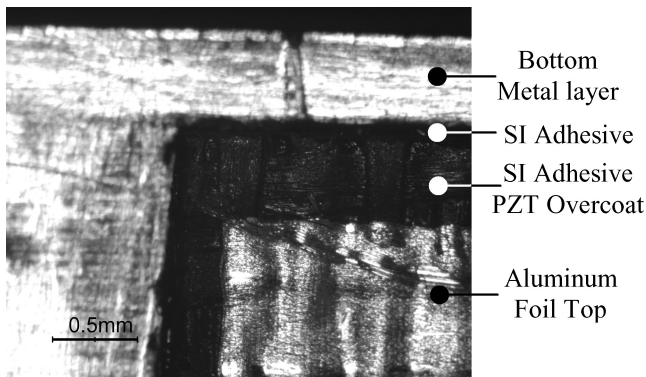


Figure 3. Top corner view of THUNDER wafer.

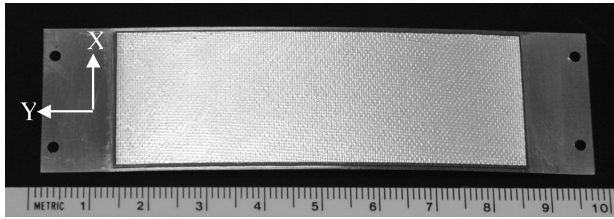


Figure 4. A THUNDER 7-Rx wafer.

Characterization Methodology

Three sets of 6 THUNDER wafers (Fig. 5) were strain gauged on the top and bottom (Fig. 6) in a pattern that allows for areal and volumetric strains to be calculated assuming X and Y axial symmetry (Fig. 6). A traveling microscope was used to measure and record the position and tilt of each gauge with the averaged position, error and tilt error from 0° , shown on Table 1.

The absolute error in position for the gauges for a given set of wafers is less than 1 mm (except YT6) which was within the coverage of the strain grid on the gauge. The angular offset error is 2.5° at the most, but typically less than 1° . To generate an off axis error in the third decimal requires an angle offset greater than 2.5° , since $\cos(2.5^\circ) = 0.999$.

The upper surface topography of a THUNDER 7-R wafer is shown in Fig. 7. The metal cutouts were covered with tape for contact scanning purposes, and these artifacts appear as covered indents near the edges parallel to the X-axis. The dominant features are the two radii of curvature, and the points near the long edge on both sides. The change in curvature along the X direction appears to be related to the location of the metal cutouts, which has an increased slope near the edges parallel to the Y-axis than in the central section of the wafer.

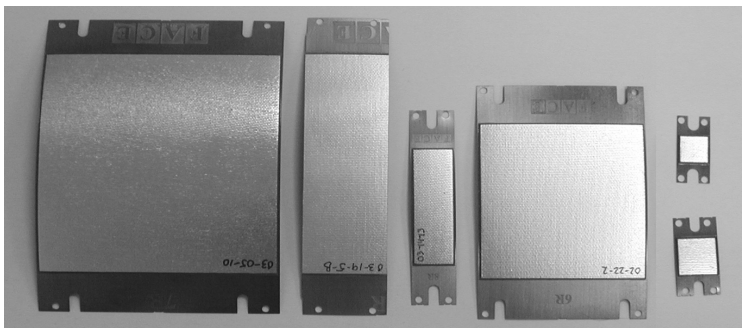


Figure 5. THUNDER wafers, left to right, top to bottom, 7-R, 7-Rx, 8-R, 6-R, 9-R and 10-R.

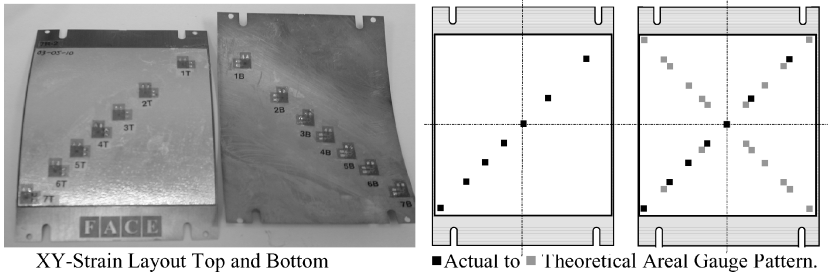


Figure 6. THUNDER 7-R with XY strain gauges.

Experimental Results

The application of both the electric field and the load was done using DC voltage levels and by suspending weights, from the load cable, to provide static behavior. The baseline test involved characterizing a set of electroded PZT-5A plates all $1.18 \text{ mm} \times 5.71 \text{ cm} \times 8.57 \text{ cm}$ (resulting dielectric constant $K_3^T \sim 1230$). These plates were strain gauged along the top and bottom, poled (2 min. at 3.5 kV/mm) and the averaged XY- (transverse and longitudinal) strains as a function of electric field were plotted (Fig. 8). Table 2 compares the experimentally determined “d” values with published commercial data [13].

When the electric field is applied to the plate in the poled Z- or d_3 direction, the ceramics display a negative strain in the XY-plane, with the apparent d_{31} constant taken as the linear slope of the experimentally determined points. As expected, the slopes are all negative and approximately equal in the d_{31} and d_{32} directions. However, the linear fit does not accurately describe the results as changes in the slopes (d values) are shown to depend on the applied electric field, and are greater than the reported low field values [14, 15]. Unlike the flat PZT plate, these bi-curved THUNDER actuators distribute their strain energy under mechanical (open and closed circuit) and electromechanical loading differently than a flat PZT plate.

The THUNDER wafers were then mounted in a test fixture (Fig. 9) that allowed for complete freedom of movement in a single cantilever configuration.

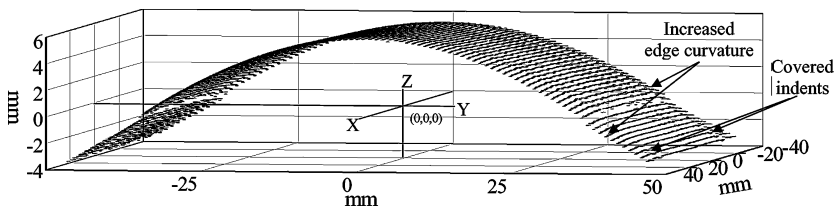


Figure 7. Upper surface topography of a THUNDER 7-R.

Table 1
Averaged XY-strain gauge location for each set of R-series THUNDER wafers

¹ Strain gauge	X ± X	Y ± Y	$\phi \pm \phi^3$	¹ Strain gauge	X ± X	Y ± Y	$\phi \pm \phi^3$	¹ Strain gauge	X ± X	Y ± Y	$\phi \pm \phi^3$
	² 6-R position (mm)				² 7-R position (mm)				² 7-Rx position (mm)		
T1	3.5 ± 0.1	2.7 ± 0.2	1.3 ± 0.1	T1	59.5 ± 2.2	60.2 ± 2.0	0.8 ± 0.8	T1	2.9 ± 0.2	2.5 ± 0.1	0.4 ± 0.1
T2	13.5 ± 0.4	12.9 ± 0.4	0.5 ± 0.3	T2	46.2 ± 0.6	46.5 ± 0.2	0.9 ± 0.7	T2	7.9 ± 0.4	20.4 ± 0.2	2.2 ± 0.9
T3	21.4 ± 0.5	20.4 ± 0.6	1.4 ± 0.1	T3	36.3 ± 0.5	35.9 ± 0.1	1.6 ± 0.6	T3	13.0 ± 0.3	35.4 ± 0.2	0.3 ± 0.1
T4	26.5 ± 0.5	25.4 ± 0.8	1.4 ± 0.1	T4	28.8 ± 0.4	28.2 ± 0.1	1.1 ± 0.7	T4	20.7 ± 0.3	45.5 ± 0.2	1.4 ± 0.2
T5	33.9 ± 0.8	33.3 ± 0.8	1.2 ± 0.4	T5	21.2 ± 0.2	20.4 ± 0.2	0.7 ± 0.3	T5	22.2 ± 1.1	66.0 ± 0.3	0.3 ± 0.2
T6	44.6 ± 0.8	43.5 ± 1.2	2.7 ± 1.9	T6	13.7 ± 0.1	13.0 ± 0.1	2.1 ± 2.0				
				T7	3.9 ± 0.08	2.9 ± 0.4	0.5 ± 0.3				
B1	2.8 ± 0.2	3.5 ± 0.2	1.3 ± 0.3	B1	60.1 ± 0.3	61.6 ± 0.3	0.2 ± 0.1	B1	2.8 ± 0.1	2.3 ± 0.3	0.5 ± 0.3
B2	12.7 ± 0.3	13.9 ± 0.2	1.4 ± 1.4	B2	44.9 ± 0.3	46.4 ± 0.3	1.1 ± 0.5	B2	7.9 ± 0.3	20.1 ± 0.3	0.4 ± 0.2
B3	20.7 ± 0.6	21.3 ± 0.5	1.1 ± 1.2	B3	34.5 ± 0.3	36.3 ± 0.4	1.2 ± 1.1	B3	13.0 ± 0.3	35.4 ± 0.2	1.0 ± 0.3
B4	25.7 ± 0.7	26.3 ± 0.5	1.2 ± 0.8	B4	26.9 ± 0.3	28.7 ± 0.5	1.1 ± 0.8	B4	20.7 ± 0.6	45.2 ± 0.3	0.7 ± 0.6
B5	33.3 ± 0.7	33.8 ± 0.6	0.3 ± 0.2	B5	19.2 ± 0.3	21.0 ± 0.6	0.4 ± 0.4	B5	15 ± 0.6	65.8 ± 0.4	1.0 ± 0.3
B6	43.7 ± 0.8	43.4 ± 0.9	0.7 ± 0.7	B6	11.6 ± 0.3	13.4 ± 0.6	0.9 ± 0.7				
				B7	1.7 ± 0.4	3.4 ± 0.7	1.2 ± 0.5				
	² 8-R position (mm)				² 9-R position (mm)				² 10-R position (mm)		
T1	3.2 ± 0.2	2.2 ± 0.4	0.9 ± 0.8	T1	3.8 ± 0.4	2.8 ± 0.2	1.6 ± 0.9	T1	3.3 ± 0.1	2.4 ± 0.1	1.3 ± 1.4
T2	4.4 ± 0.3	9.7 ± 0.4	2.1 ± 2.5					T2	8.4 ± 0.3	7.4 ± 0.2	0.5 ± 0.2
T3	6.6 ± 0.2	19.1 ± 0.5	1.4 ± 0.4								
T4	7.6 ± 0.4	33.2 ± 0.3	1.3 ± 0.9								
B1	2.9 ± 0.4	2.5 ± 0.6	1.9 ± 0.2	B1	3.8 ± 0.1	2.9 ± 0.1	2.7 ± 1.4	B1	3.3 ± 0.5	2.7 ± 0.5	0.9 ± 0.9
B2	4.1 ± 0.5	10.1 ± 0.9	1.8 ± 1.3					B2	8.3 ± 0.3	7.3 ± 0.3	2.1 ± 1.6
B3	6.4 ± 0.2	19.1 ± 0.8	0.2 ± 0.1								
B4	7.7 ± 0.4	33.0 ± 0.8	0.5 ± 0.5								

¹T = top, B = bottom.

²Origin (0,0) is from corner of ceramic, measurements are in XY-plane.

³XY angle offset from 0/90°.

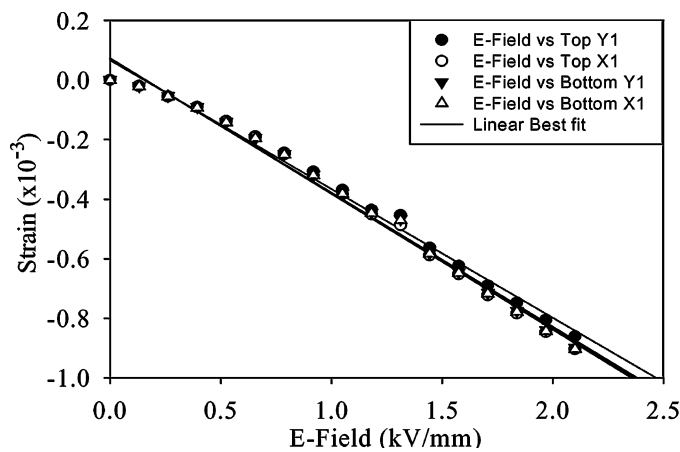


Figure 8. Averaged strain versus applied electric field on three PZT-5A type ceramic plates.

The test station allowed simultaneous recording of center displacements, via LVDT, and transverse (X-axis) and longitudinal (Y-axis) strains, via XY-gauges, during the application of electric fields or uniformly distributed mechanical loads. Both the application of electric field (positive in poled direction) and mechanical load (longitudinal) cause the THUNDER actuators to displace in the negative Z direction. This allowed for direct strain comparisons between pure tensile mechanical and applied electrical loads.

The following Figs. 10a–f illustrate the experimental results of the center displacements as a function of applied DC electric field (no load) and loads (no applied electric field) for each set of three THUNDER actuators tested (Fig. 5). The results of the inverse slopes of these plots are presented on Table 3.

The plots (Figs. 10a–f) and tabular data (Table 3) show that there is no discernable difference between the loaded open and short circuit on the center displacement of each THUNDER actuator. This is surprising since there is a

Table 2
Reference vs. experimental data

¹ PZT-5A manufacture	$d_{31} \ (\times 10^{-12} \text{ m/V})$
² CTS Corp	-450 ± 10
CTS Corp	-190 (3195HD)
Morgan Matroc	-171 (PZT5A3)

¹Ref 13.

²This work.

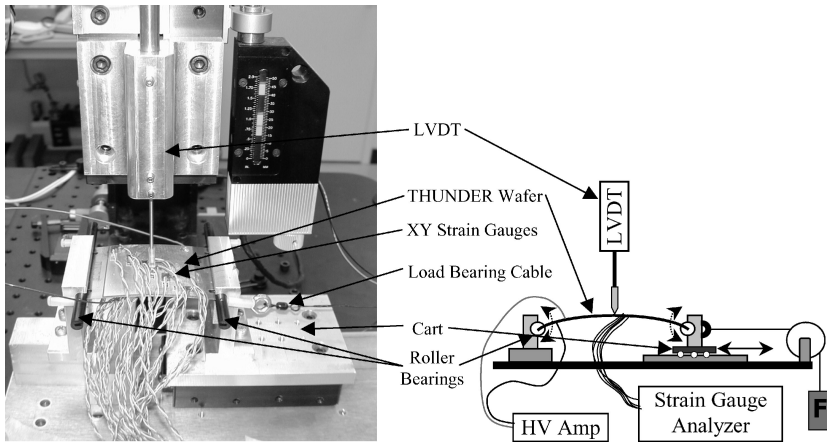


Figure 9. Wafer test station and diagram.

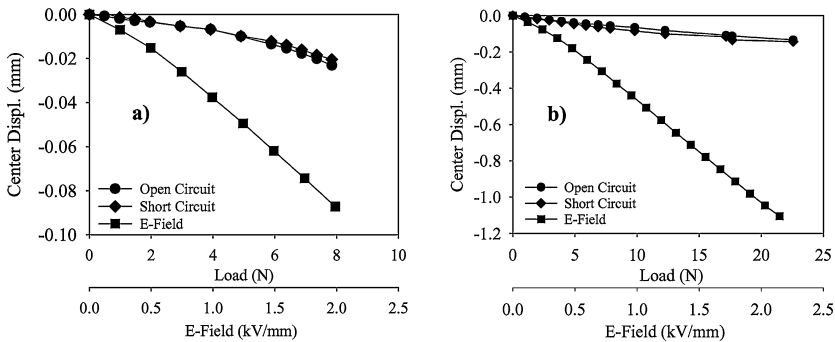


Figure 10a–b. Center displacement vs. load and E-field for (a) 9-R, (b) 10-R.

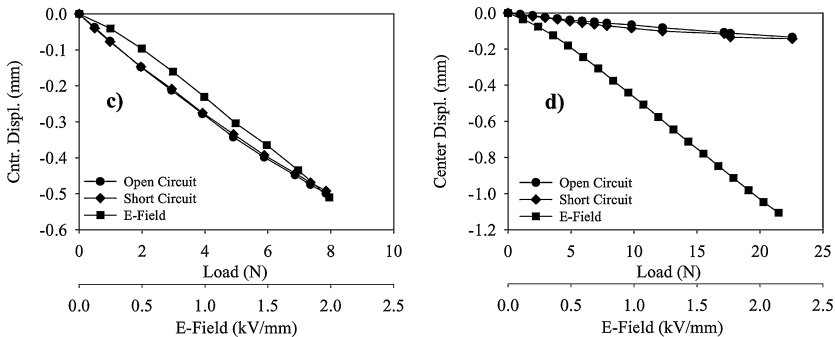


Figure 10c–d. Center displacement vs. load and E-field for (c) 8-R, (d) 6-R.

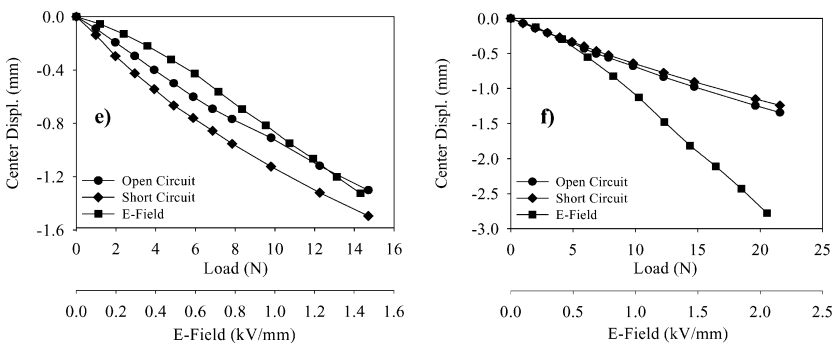


Figure 10e-f. Center displacement vs. load and E-field for (e) 7-R and (f) 7-Rx.

difference in the open and closed circuit elastic constants (modulus and compliance) in the PZT ceramic, especially in the poled direction. This behavior suggests that the stiffness of the device dominates the change in the electro-mechanical properties of the ceramic. The plots of center displacement versus electric field demonstrate that this device displaces several orders of magnitude beyond that of the base PZT plate. Since the large displacement is partially a function of geometry, the base “ d_{xx} ” values of the ceramic should only be used as indicators to determine how the final device may function. The inverse slopes of these plots give the open and closed circuit mechanical spring constants and the electric field per linear displacement; these values are summarized on Table 3. In comparison, the THUNDER actuators that are thicker, shorter in length and square have greater spring constants and require increased electrical fields to move a set distance.

The next task was to plot the averaged areal strains as a function of applied load and electric field for each set of actuators. Table 4 serves as a key to

Table 3
Calculated inverted linear slopes of plots in Figs. 10a–f

THUNDER	$L \times W \times D$ (mm)	¹ Open circuit “k” (N/mm)	¹ Short circuit “k” (N/mm)	² E-field “D” (kV/mm ²)
6-R	76.2 × 50.8 × 0.78	−168	−149	−1.85
7-R	96.5 × 71.1 × 0.58	−15.9	−16.3	−0.71
7-Rx	96.5 × 25.4 × 0.58	−11.2	−10	−1.04
8-R	63.5 × 12.7 × 0.48	−15.7	−15.7	−3.85
9-R	22.3 × 9.6 × 0.53	−206	−203	−66.2
10-R	25.4 × 12.7 × 0.73	−361	−389	−22.4

¹F = kx, Spring Constant “k.”

²E = Dx, Center Displacement Constant “D.”

Table 4
Symbol reference for Figs. 12–16

Descriptor	Symbol	TH 6-R	TH 7-R	TH 7-Rx	TH 8-R	TH 9-R	TH 10-R
S.G. YT1/XT1	●						
S.G. YT2/XT2	▼						
S.G. YT3/XT3	■						
S.G. YT4/XT4	◆						
S.G. YT5/XT5	▲						
S.G. YT6/XT6	△						
S.G. YT7/XT7	★						
S.G. YB1/XB1	○						
S.G. YB2/XB2	▽						
S.G. YB3/XB3	□						
S.G. YB4/XB4	◇						
S.G. YB5/XB5	△						
S.G. YB6/XB6	○						
S.G. YB7/XB7	★						

S.G. = Strain Gauge, Y = Longitudinal axis, X = Traverse axis, T = Top, B = Bottom, # corresponds to gauge.

Figs. 12–16 (Fig. 11 key is shown below plots) with the actual gauge locations and offset angles shown earlier on Table 1.

The plots in Figs. 11–16 show the strain across the diagonal surfaces of the THUNDER actuators, with non-fitted lines connecting the points. There are several load versus strain plots, Figs. 11 and 12, where the maximum strains do not exceed 25 ppm ($\times 10^{-6}$) and appear random. The data from these plots can be summarized as strains signals low enough to be noisy. The standard deviation, between specimens with strains above 100 ppm is $\pm 20\%$ with the deviation decreasing to $\pm 10\%$ as the strains approach 1000 ppm. These latter deviations are most likely caused by variations in THUNDER processing, as the gauge signal to noise ratio is increased at higher strain output. In nearly all cases, the short and open circuit strains versus load plots are almost identical, as previously shown in Fig. 10. Again, this is surprising since the actual surface strains are much more sensitive to changes in strain, as a function of the change in stiffness due to surface charging effects, than the center displacement.

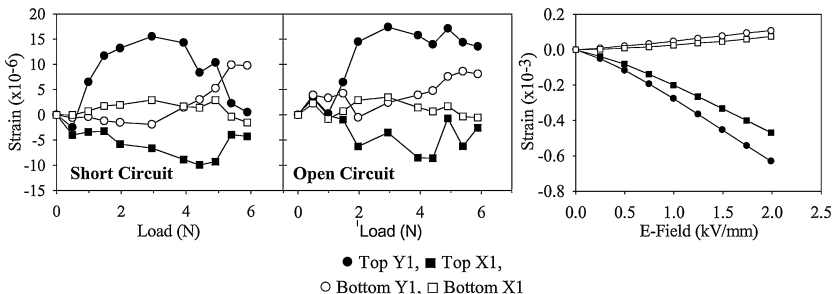


Figure 11. THUNDER 9-R, XY-strain as a function of applied load and E-field.

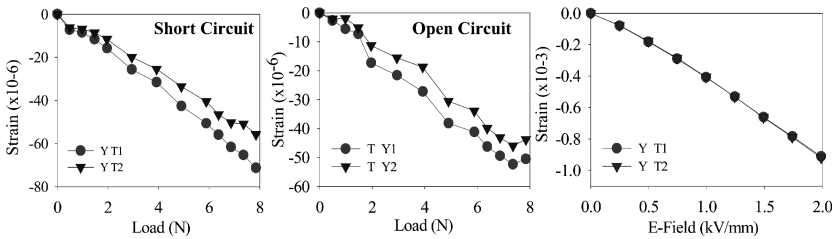


Figure 12a. THUNDER 10-R, top Y-strain as a function of applied load and E-field.

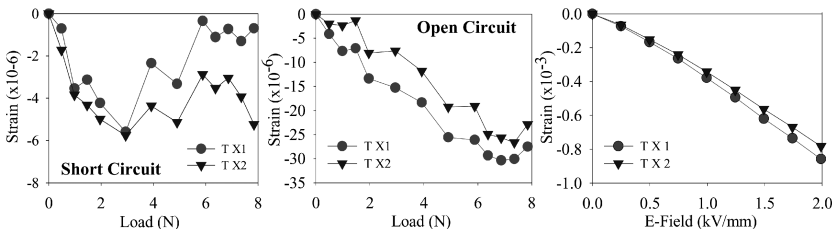


Figure 12b. THUNDER 10-R, top X-strain as a function of applied load and E-field.

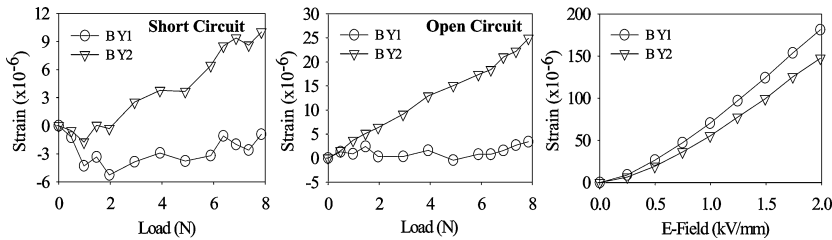


Figure 12c. THUNDER 10-R, bottom Y-strain as a function of applied load and E-field.

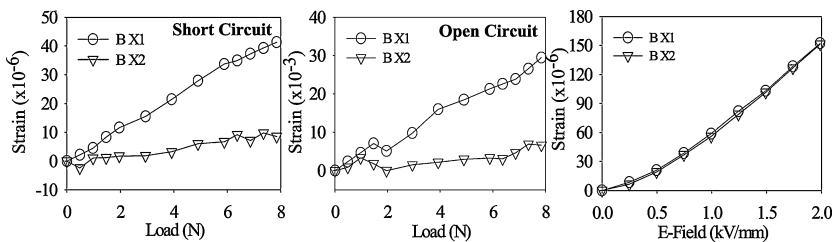


Figure 12d. THUNDER 10-R, bottom X-strain as a function of applied load and E-field.

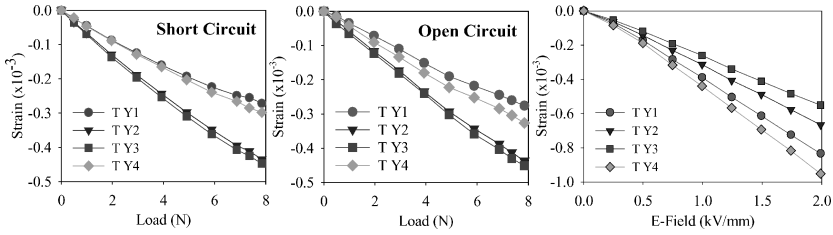


Figure 13a. THUNDER 8-R, top Y-strain as a function of applied load and E-field.

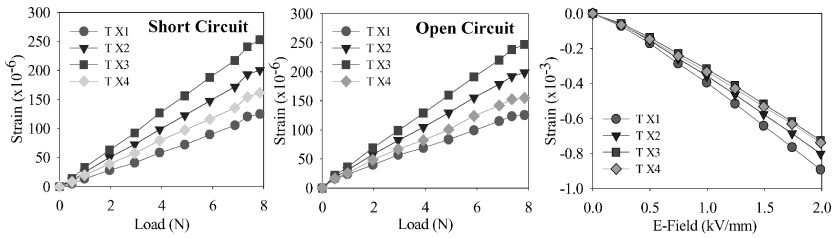


Figure 13b. THUNDER 8-R, top X-strain as a function of applied load and E-field.

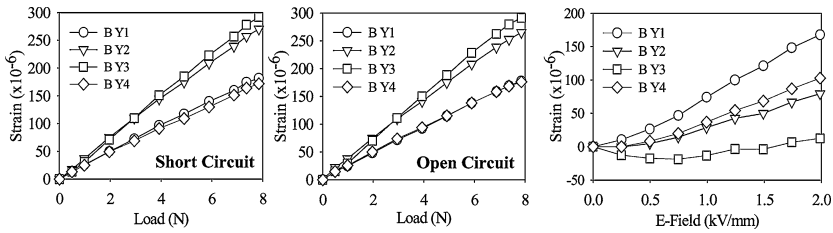


Figure 13c. THUNDER 8-R, bottom Y-strain as a function of applied load and E-field.

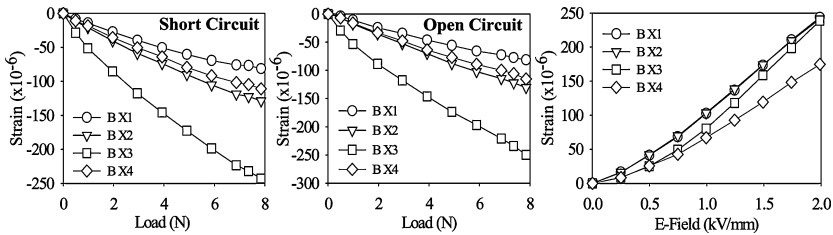


Figure 13d. THUNDER 8-R, bottom X-strain as a function of applied load and E-field.

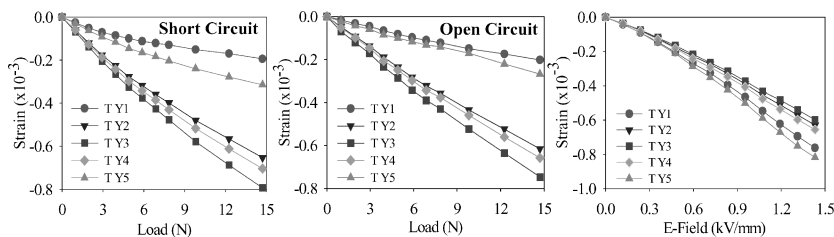


Figure 14a. THUNDER 7-Rx, top Y-strain as a function of applied load and E-field.

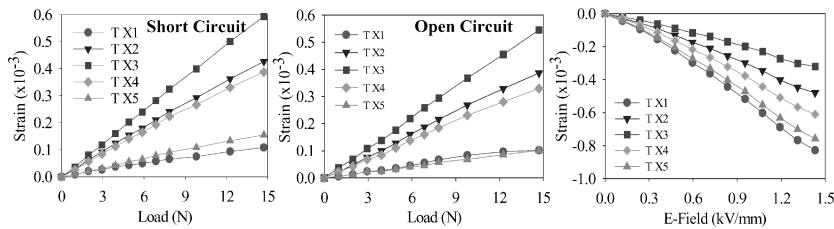


Figure 14b. THUNDER 7-Rx, top X-strain as a function of applied load and E-field.

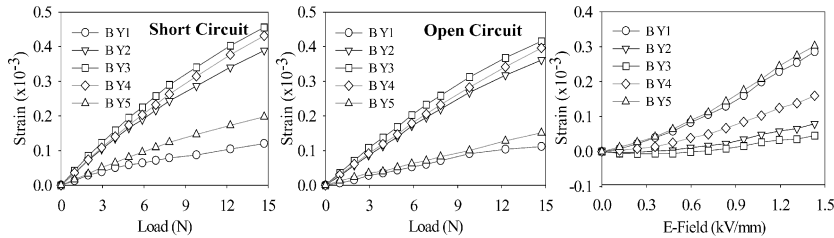


Figure 14c. THUNDER 7-Rx, bottom Y-strain as a function of applied load and E-field.

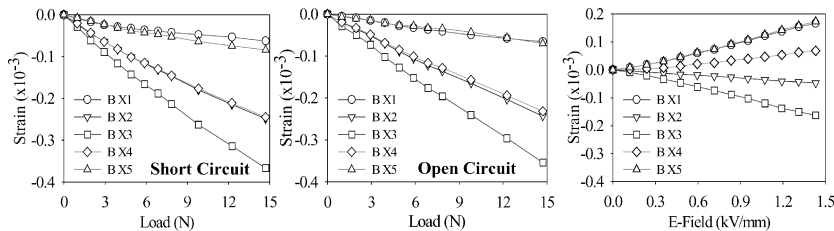


Figure 14d. THUNDER 7-Rx, bottom X-strain as a function of applied load and E-field.

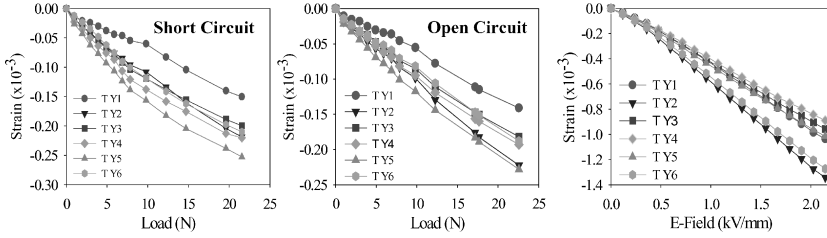


Figure 15a. THUNDER 6-R, top Y-strain as a function of load and E-field.

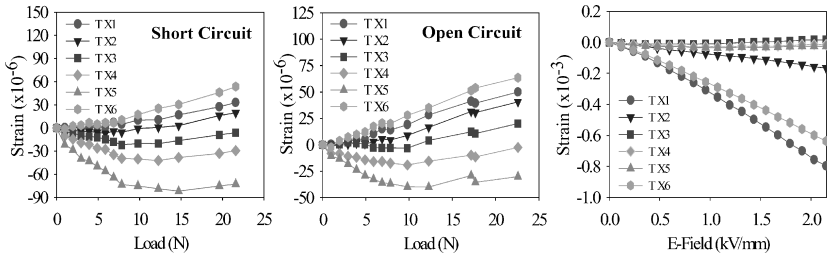


Figure 15b. THUNDER 6-R, top X-strain as a function of load and E-field.

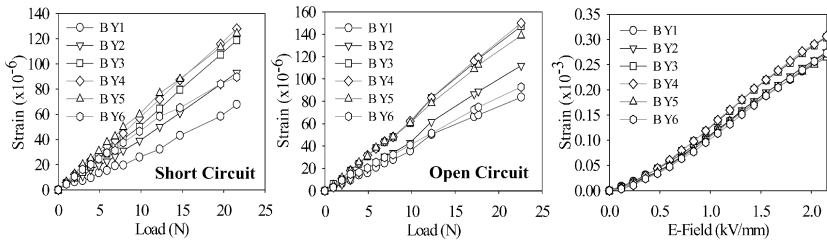


Figure 15c. THUNDER 6-R, bottom Y-strain as a function of load and E-field.

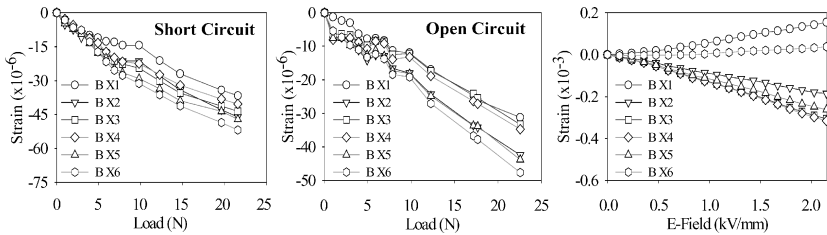


Figure 15d. THUNDER 6-R, bottom X-strain as a function of load and E-field.

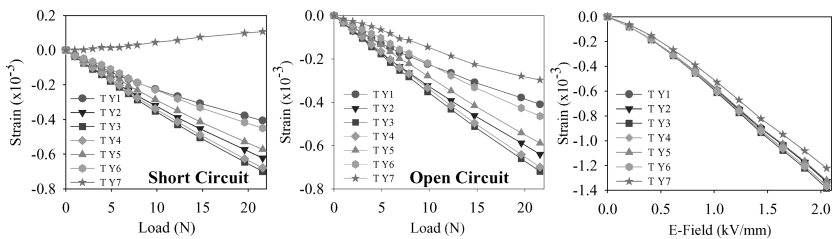


Figure 16a. THUNDER 7-R, top Y-strain as a function of applied load and E-field.

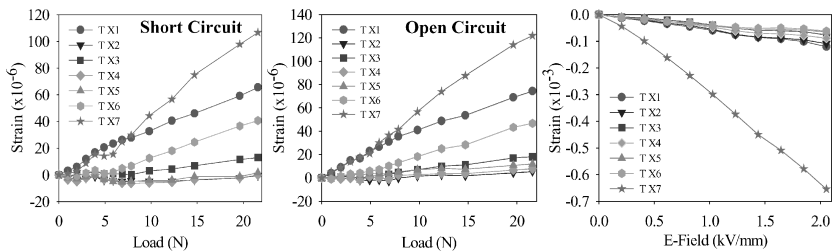


Figure 16b. THUNDER 7-R, top X-strain as a function of applied load and E-field.

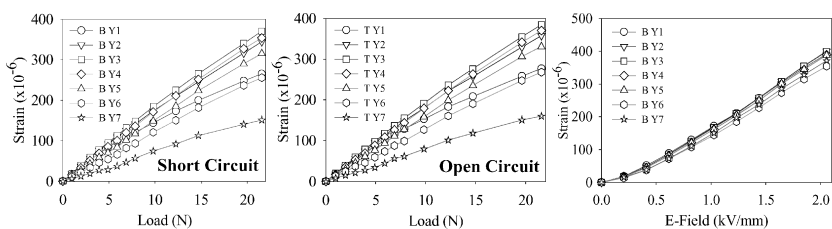


Figure 16c. THUNDER 7-R, bottom Y-strain as a function of applied load and E-field.

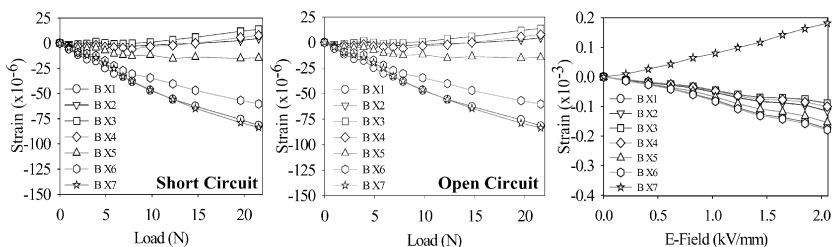


Figure 16d. THUNDER 7-R, bottom X-strain as a function of applied load and E-Field.

When comparing the slopes of the short and open circuit strain versus load plots, the top longitudinal (lengthwise Y) strains are negative, in compression, while the corresponding bottom Y strains are positive, in tension. The top traverse (widthwise X) strains are positive, in tension, and the bottom X strains are in compression. In the cases where the THUNDER is mostly rectangular, 7-Rx and 8-R, the gauges in the middle of the actuator experience greater strains than those at the ends. When the THUNDER ceramic is symmetrically square, all the longitudinal strains are comparable with the edge strains tending towards lower strain values (THUNDER 6-R). The THUNDER 7-R shows similar behavior, except that the edges are straining differently where the T and BX7 gauges are located. This is most likely caused by the placement of the metal mounting cutouts (see Figs. 5–7) that cause the actuator to have an accented transverse bend near the edges. THUNDER 10-R has both gauges mounted off center and with corresponding low strain level. Hence, this data was not assessed beyond the recorded values. When the THUNDER actuator is evenly loaded and characterized as a spring, the strain field indicates that the device is curving cylindrically, with its long axis lengthwise, as the tension is increased, rather than becoming a flat plate. However, the geometric and material constraints do not allow this device to buckle into a cylinder, without fracturing the ceramic. Thus, the geometry of the THUNDER actuator shifts between two cylindrical forms that become curved about the Y or X axis depending on applied tension or compression. This behavior was shown though calculations done by Ochirero and Hyer [16].

The strains generated by the electric field are greater than those examined under tensile loads. This is because the ceramic is now straining the THUNDER device along its 3 principal axes rather than responding to a single axis loading stress. The general trend is that the upper surfaces strain opposite those on the bottom surface, depending on the area geometry or the stiffness of the pre-stress layer. It would be expected that both surfaces would be in compression, as demonstrated with the flat plates (see Fig. 9), but the differential prestress through the vertical Z-axis appears to effect ceramic surfaces as being poled opposite. Again, the edge effect on the T and BX7 strain outputs for the THUNDER 7-R are different than what would be expected for a smoothly contoured wafer. The strain field generated by the electrical field is different than that caused by loading the actuator in tension. Both cases appear to uniformly strain the device if center displacement is the only characterization criteria.

The last task was to fit linear slopes to plots in the Figs. 11–16 as a function of the gauge number, which is related to the linear diagonal distance across the top and bottom of the THUNDER actuator. Viewing the data in this manner affords a qualitative assessment of the areal strain distribution across both actuator surfaces (Figs. 17–22) with the first bar in each set being the top surface strain gauge.

The strain/load bar graphs in Fig. 17 are of the slopes where the strain gauges were noisy, while Fig. 18 does not have enough gauge points to draw

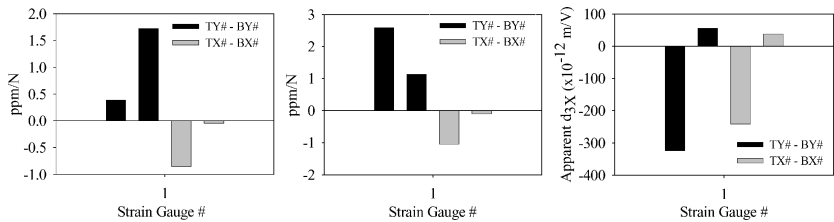


Figure 17. THUNDER 9-R, linear slopes of strain/load and strain/E-field plots versus strain gauge number.

valid conclusions. The rest of the load plots (Figs. 19–22) show a similar trend where the top and bottom center parts of the wafers are strained more in the longitudinal (tensile) direction than the ends. However, the transversely loaded direction shows greater center strains with the rectangular THUNDERS (7-RX and 8-R) where as the square wafers tend to be strained more at each end (6-R and 7-R). The wafer 10-R displays similar trends in that the top and bottom Y gauges are strained opposite, while the top and bottom X gauges are strained in a manner similar to the electric field plot. The strain/electric field plots, like Fig. 9, are the apparent d_{3X} values, taken at discrete locations and directions along the actuator surface. These values resolve into effective “ d_{31} ” and “ d_{32} ” constants in the longitudinal “Y” and transverse “X” directions, respectively. The rectangular THUNDERS (7-RX and 8-R) display the highest strain levels at the ends, whereas the corresponding 6-R and 7-R values appear to be more consistent. For the transverse strains, the 8-R values appear to be nearly equal with the topside completely in compression and the bottom fully in tension. The other rectangular THUNDER 7-R appears to go almost completely in compression about its center, except longitudinally across the bottom with the ends in tension in the transverse direction. The square THUNDERS, 6-R and 7-R tend to remain in compression transversely, except for the edges which may be influenced by the metal cutouts. Lastly, the location of a neutral strain axis can be qualitatively realized by balancing tension and compression

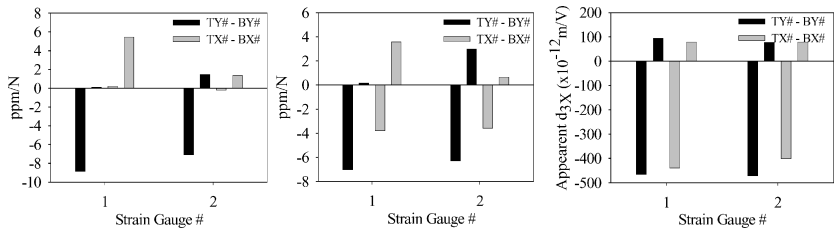


Figure 18. THUNDER 10-R, linear slopes of strain/load and strain/E-field plots versus strain gauge number.

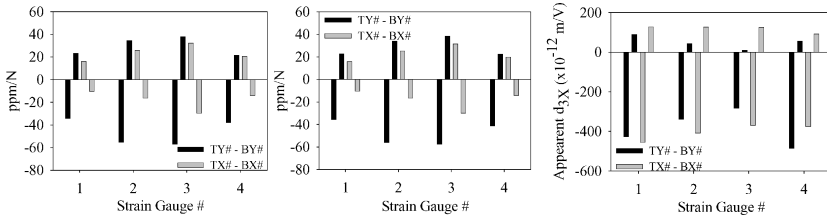


Figure 19. THUNDER 8-R, linear slopes of strain/load and strain/E-field plots versus strain gauge number.

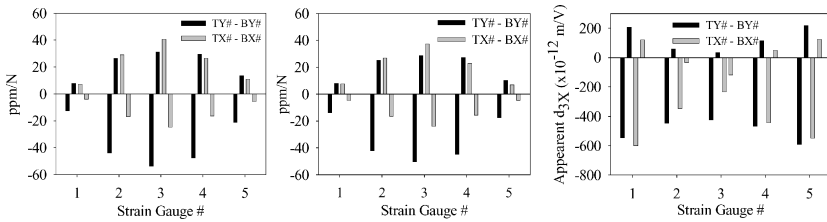


Figure 20. THUNDER 7-RX, linear slopes of strain/load and strain/E-field plots versus strain gauge number.

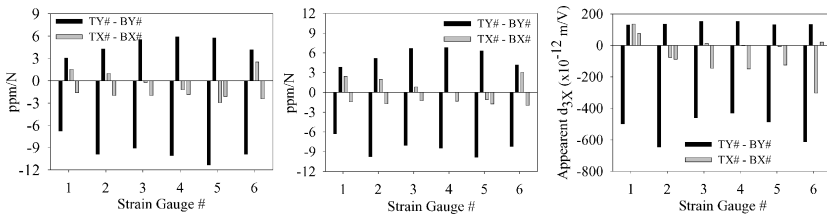


Figure 21. THUNDER 6-R, linear slopes of strain/load and strain/E-field plots versus strain gauge number.

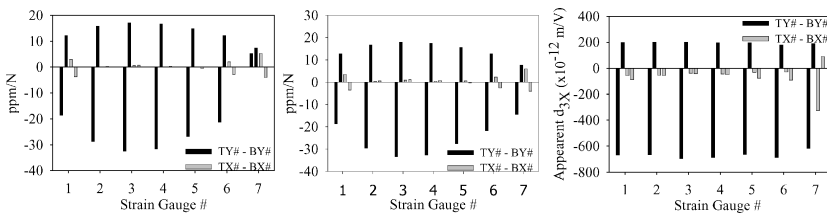


Figure 22. THUNDER 7-R, linear slopes of strain/load and strain/E-field plots versus strain gauge number.

bars in the longitudinal and transverse directions. Hence, the strain/load and strain/electric field versus strain gauge number indicate that the general tension and compression trends are similar in terms of tension and compression, but the overall areal characteristics are different in terms of the load distribution.

CONCLUSIONS

The THUNDER device is a complex laminate system where materials that span several orders of modulus, CTE and viscoelasticity are in intimate contact and must operate in a simultaneous fashion. Thus, behavior of prestressed THUNDER actuators is drastically different than the piezoceramic that serves as the active element. Hence, the standard methods of characterization used to obtain values of well behaved ceramic shapes only offer marginal indications of the resulting THUNDER performance. The THUNDER devices are linear in their behavior when they are characterized as devices rather than materials. Parameters such as an effective spring constant "k" and "D" coefficient were experimentally determined by the use of a LVDT, and the apparent d_{31} values were obtained with strategically located strain gauges. The results show a range of values of effective spring constants for the range of Thunder devices tested from 10 to 389 N/mm for an open and short circuit test, D coefficients values ranged from 0.7 to 66.0 KV/mm² with experimentally determined d_{31} values ranging from over -700 to 400×10^{-12} m/V. Although THUNDER actuators are a challenge to characterize, they offer many unique abilities for piezoelectric actuator applications, due to their design variability. For instance, there are some areas where the strain is nearly zero throughout the application of the electric field to some of these wafers. These neutral points might serve as an area to place an insert on or through the device. However, the effect of loading combined with the application of an electric field needs to be determined in order to validate this assumption. Then, it should be possible to design an actuator that is slightly strained under heavy preloads, and can perform extremely well under these conditions. However, without proper experimental verification, the current computational piezoelectric models cannot be accurately scaled to address complex engineering problems.

REFERENCES

1. K. M. Mossi, G. V. Selby, and R. G. Bryant, *Materials Letters* **35**(1), 39–49 (1998).
2. R. F. Hellbaum, R. G. Bryant, R. L. Fox, *et al.*, US Patents 5,632,841 (1997), 6,060,811 (2000), 6,734,603 B2 (2004), European Patent EP 0 819 048 B1 (2003) all to NASA.
3. Soon W. Chung and Seung J. Kim, Proc. SPIE; Smart Structures and Materials: Smart Structures and Integrated Systems, 5056, Amir M. Baz, ed., pp. 247–254 (2003).

4. Robert Wieman, Ralph C. Smith, Tyson Kackley, Zoubaida Ounaies, and Jeffrey D. Bernd, Proc. SPIE; Smart Structures and Materials: Modeling, Signal Processing, and Control in Smart Structures, 4326, Vittal S. Rao, ed., pp. 252–263 (2001).
5. Barmac K. Taleghani, Proc. SPIE: Fifth European Conference on Smart Structures and Materials, 4073, Pierre F. Gobin, Clifford M. Friend, eds., pp. 37–45 (2000).
6. Jun K. Song and Gregory N. Washington, Proc. SPIE; Smart Structures and Materials: Smart Structures and Integrated Systems, 3668, Norman M. Wereley, ed., pp. 866–877 (1999).
7. Barmac K. Taleghani, and Joel F. Campbell, Proc. SPIE, Smart Structures and Materials 1999: Smart Structures and Integrated Systems; 3668, Norman M. Wereley, ed., pp. 555–566 (1999).
8. M. Capozzoli, J. Gopalakrishnan, K. Hogan, Jordan E. Massad, T. Tokarchik, Stephen Wilmarth, H. Thomas Banks, Karla M. Mossi, and Ralph C. Smith, Proc. SPIE: Smart Structures and Materials 1999: Mathematics and Control in Smart Structures, 3667, Vasundara V. Varadan, ed., pp. 719–727 (1999).
9. M. W. Hyer and A. Jilani, *Smart Mater. Struct.* **7**(6), 784–791 (1998).
10. Robert W. Schwartz, Pitak Laoratanakul, William D. Nothwang, John Ballato, Youngwoo Moon, and Alison Jackson, Proc. SPIE—The International Society for Optical Engineering 3992, pp. 363–375 (2000).
11. R. W. Schwartz and M. Narayanan, *Sensors and Actuators, A: Physical* **101**(3), 322–331 (2002).
12. <http://www.face-int.com/pdf/whtpaper.pdf> and <http://www.face-int.com/pdf/appnotes.pdf>
13. <http://www.ctscorp.com/components/Datasheets/PZT.pdf> and <http://www.morganelectroceramics.com/proptables.pdf>
14. W. Ren, A. J. Masys, G. Yang and B. K. Mukherjee, 3rd Asian meeting on Ferroelectrics (AMF3), Hong Kong, December 12 (2000).
15. J. Erhart and L. Burianová, *J. European Ceramic Soc.* **21**, 1413 (2001).
16. T. T. Ochinerio and M. W. Hyer, *Journal of Thermoplastic Composite Materials* **15**(2), 79–87 (2002).